POLITECNICO DI TORINO
Repository ISTITUZIONALE

Operando pH measurements decipher H+/Zn2+intercalation chemistry in high-performance aqueous Zn/-V2O5batteries

Original
Operando pH measurements decipher H+/Zn2+intercalation chemistry in high-performance aqueous Zn/-V2O5batteries / Liu, X.; Euchner, H.; Zarrabeitia, M.; Gao, X.; Elia, G. A.; Gross, A.; Passerini, S.. - In: ACS ENERGY LETTERS. - ISSN 2380-8195. - ELETTRONICO. - 5:9(2020), pp. 2979-2986. [10.1021/acsenergylett.0c01767]

Availability:
This version is available at: 11583/2959184 since: 2022-04-13T10:19:53Z

Publisher:
American Chemical Society

Published
DOI:10.1021/acsenergylett.0c01767

Terms of use:

This article is made available under terms and conditions as specified in the corresponding bibliographic description in the repository

Publisher copyright
GENERICO -- per es. Nature : semplice rinvio dal preprint/submitted, o postprint/AAM [ex default]

(Article begins on next page)

25 April 2024

Occurrence of H^+/Zn^{2+} Exchange in High-Performance Aqueous Zn/δ-$Ca_{0.24}V_2O_5$ Intercalation Batteries

Xu Liu,[1,2] Holger Euchner,[1] Maider Zarrabeitia,[1,2,3] Xinpei Gao,[1,2] Giuseppe Antonio Elia,[1,2] Axel Groß,[1,4] Stefano Passerini[1,2]**

[1] Helmholtz Institute Ulm (HIU), Helmholtzstrasse 11, D-89081 Ulm, Germany

[2] Karlsruhe Institute of Technology (KIT), P.O. Box 3640, D-76021 Karlsruhe, Germany

3 Centre for Cooperative Research on Alternative Energies (CIC energiGUNE), Basque Research and Technology Alliance (BRTA), Alava Technology Park, Albert Einstein 48, 01510 Vitoria-Gasteiz, Spain

4. University of Ulm, Institute of Theoretical Chemistry, Albert-Einstein-Allee 11, D-89081 Ulm, Germany

Corresponding Authors

*E-mail: giuseppe.elia@kit.edu; stefano.passerini@kit.edu

ABSTRACT

Vanadium oxides have been recognized among the most promising positive electrode materials for aqueous zinc metal batteries (AZMBs). However, their underlying intercalation mechanisms are still debated. To shed light on the intercalation mechanisms, high-performance δ-$Ca_{0.24}V_2O_5$/GO (357 mAh g^{-1} at 50mA g^{-1}) is investigated as a model compound. Its structural and electrochemical behaviors in the designed cells with three different electrolytes, e.g., 3 m $Zn(CF_3SO_3)_2$/water, 0.01 M H_2SO_4/water, and 1 M $Zn(CF_3SO_3)_2$/acetonitrile, demonstrate that the conventional structural and elemental characterization methods cannot adequately clarify the respective role of H^+ and Zn^{2+} intercalations in the $Zn(CF_3SO_3)_2$/water electrolyte. Thus, an *operando* pH determination method is developed and used for the first time toward Zn/vanadium oxide AZMBs. It witnesses the intercalation of both H^+ and Zn^{2+} into CVO and uncovers an unusual H^+/Zn^{2+}-exchange intercalation/de-intercalation mechanism. Density functional theory calculations further reveal that such the exchange is a consequence of the variation of the electrochemical potential of Zn^{2+} and H^+ during the electrochemical intercalation/release.

TOC GRAPHICS

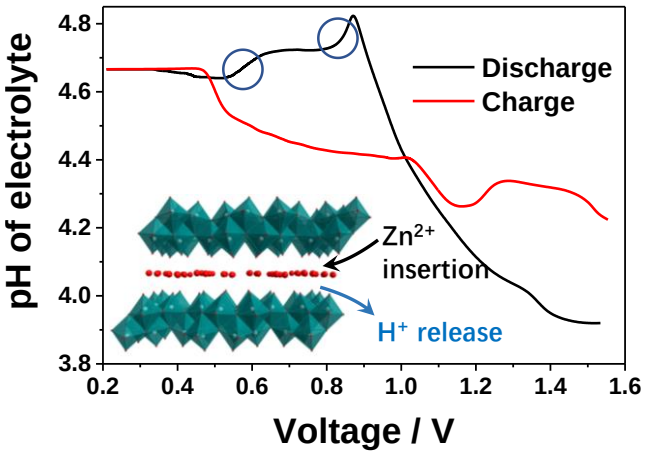

Aqueous zinc metal batteries (AZMBs) are a promising complementary technology to the state-of-the-art lithium-ion batteries for large-scale stationary energy storage due to their sustainability,[1] low cost,[2] safety,[3,4] and high energy density among aqueous batteries[5–7]. Since σ-$Zn_{0.25}V_2O_5$ was employed as an intercalation-type cathode material for AZMBs in 2016,[8] vanadium oxides have been extensively investigated.[3,9,10] The R&D efforts resulted in the rational design of their structure,[11,12] morphology,[13,14], and addition of secondary components,[15,16] enabling high specific capacities (more than 300 mAh g^{-1} at 50 mA g^{-1}) and prolonged cycle life (hundreds of cycles at 500 mA g^{-1}).[4,17] Nevertheless, the fundamental questions, i.e., which/how species are intercalated into these vanadium oxides, are still controversially debated.

Although many different characterizations were used in the studies mentioned above, typically, X-ray diffraction (XRD) was the main tool providing the evidence supporting the respective mechanisms. During the operation of many reported vanadium oxides,[7,8,18–29] two main phenomena, reversible peak shifts of the initial phase, and reversible appearances of basic zinc salts (BZSs) at low potentials are often observed in the XRD patterns. Different explanations proposed in the literature for these phenomena give rise to the different intercalation mechanisms, including H^+,[21] Zn^{2+},[7] and their combination.[25] The peak shifts indicate solid solution processes, going along with a changing interlayer distance. Zn^{2+}, the main cation in the commonly used aqueous electrolytes, is considered responsible for the shrinking interlayer distance during the discharge process.[8,22,23,29] However, the possibility of H^+ intercalation, which could also contribute to the interlayer shrinking, is neglected. The appearances of BZSs upon discharge are dependent on the employed electrolytes. For example in $ZnSO_4$ based electrolyte, $Zn_4SO_4(OH)_6$,[19,21,30] $Zn_{12}(CF_3SO_3)_9(OH)_{15}$,[31,32] $Zn_4ClO_4(OH)_7 \cdot xH_2O$,[33] and $Zn_5(OH)_8Cl_2$[28] BZSs are formed, while different BZSs are present employing $Zn(CF_3SO_3)_2$ ($Zn(OTF)_2$), $Zn(ClO_4)_2$, and $ZnCl_2$ based

aqueous electrolytes. These compounds precipitate during the discharge process, disappearing upon charge. BZSs formation is induced by pH variation of the electrolyte; hence, they have been recognized to be an indicator for the reversible H^+ intercalation.[19,30] Thereafter, the Zn^{2+} intercalation process was widely doubted by the scientific community,[34] as the intercalation of multivalent cations had been believed to be difficult and sluggish,[35] whereas vanadium oxides exhibited a decent specific capacity and rate capability in AZMBs. For example, Li et al. attributed the capacity of VO_2 in $ZnSO_4$ aqueous electrolyte to the H^+ intercalation.[21] Apparently, the role of H^+ and Zn^{2+} intercalations in the vanadium oxides-based AZMBs still needs to be clarified, requiring further experimental evidence. Deciphering the intercalated carriers is not trivial and may guide scientists further to optimize cathode materials and electrolytes for better performing AZMBs.

In this work, high-performance δ-$Ca_{0.24}V_2O_5$/GO (CVO/GO) was used as a model compound to investigate the widely explored but still debated intercalation mechanism. The intercalation of either H^+ or Zn^{2+} was investigated via the designed cells with 0.01 M H_2SO_4/water and 1 M $Zn(OTF)_2$/ACN electrolytes, respectively. The obtained results reveal that the conventional structural and elemental characterization methods cannot adequately clarify the respective role of H^+ and Zn^{2+} intercalations in the $Zn(OTF)_2$/water electrolyte. Thus, *operando* pH measurements were developed to investigate the intercalation process. A thereby uncovered H^+/Zn^{2+}-exchange intercalation chemistry, in which the Zn^{2+} intercalation/release is accompanied with H^+ release/intercalation, respectively, was further corroborated via DFT calculations.

CVO/GO was prepared via an efficient microwave reaction through which the reaction can be finished in 2 h at 180 °C. This preparation method for δ-V_2O_5 has not been reported before, but its efficiency is much higher than other δ-V_2O_5 synthesis routes generally requiring several steps and

tens of hours.[28,36–39] More details about the preparation can be found in the Supporting Information (SI, experimental details, and Figure S1). The XRD refinement of the as-prepared sample demonstrates that the δ-$Ca_{0.24}V_2O_5$ with an interlayer distance of 10.6 Å was obtained (Fig. 1a). Its crystal structure is depicted in the inset of Fig. 1a. As seen in the scanning electron microscope (SEM) images and energy-dispersive X-ray spectroscopy (EDS) mapping of the CVO/GO (Fig. 1b and Fig. S2, respectively), the sub-micrometer rods of CVO are anchored on the surface of the micro GO sheets.

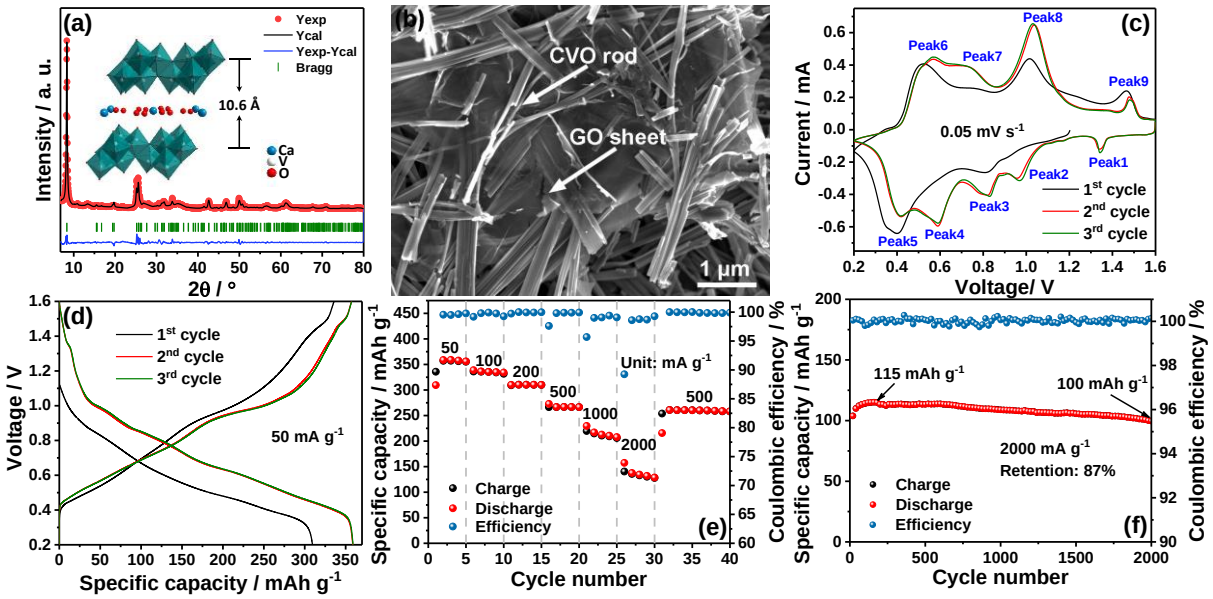

Figure 1. *(a) XRD refinement of as-prepared CVO/GO and the crystal structure model of $Ca_{0.24}V_2O_5{\cdot}H_2O$. (b) SEM images of as-prepared CVO/GO. (c-f): Electrochemical performance of the as-fabricated CVO/GO electrode. (c) CV curves measured at 0.05 mV s^{-1}. (d) Charge/discharge profiles at 50 mA g^{-1}. (e) Specific capacity and Coulombic efficiency obtained at different specific currents. (f) Specific capacity and Coulombic efficiency up cycling at 2000 mA g^{-1}. Coin cell, 3 m Zn(OTF)2 aqueous electrolyte.*

The electrochemical performance of as-prepared CVO/GO as cathode material for AZMBs was evaluated in coin cells employing a zinc foil as the negative electrode and a 3 m $Zn(OTF)_2$ aqueous solution as the electrolyte. Fig. 1c displays the cyclic voltammetry (CV) curves measured at a scan

rate of 0.05 mV s^{-1}. The first cycle is different from those following, indicating an activation process to occur. Also, the presence of multiple peaks indicates a multistep electrochemical process. Galvanostatic cycling with potential limitation (GCPL) tests were employed to evaluate the storage capacity. The charge/discharge profiles recorded during the initial three cycles (at 50 mA g^{-1}) are displayed in Fig. 1d. In agreement with the CV results, there is an evident increase in the delivered capacity after the first cycle showing a charge capacity higher than the discharge capacity. However, a highly reversible behavior is observed in the following two cycles in which a specific capacity of 357 mAh g^{-1} is delivered. The different electrochemical response in the first cycle is most likely the result of the de-intercalation of calcium ions from CVO, occurring upon the first charge above 1.2 V. This is strongly corroborated by XPS measurements which demonstrate a significant decrease of the relative signal intensity of Ca 2p against V 2p after the first cycle (Fig. S3).[28] The specific capacity at various current densities, measured via GCPL, are displayed in Fig. 1e. At specific currents of 500 and 1000 mA g^{-1}, specific capacities of 267 and 215 mAh g^{-1} are delivered, respectively. The cyclability of CVO/GO was also estimated using GCPL. After 200 cycles at 500 mA g^{-1} (Fig. S4) and 2000 cycles at 2000 mA g^{-1} (Fig. 1f), the cell retains 92% and 87% of the initial capacities, respectively, thus showing a good cyclability. The charge/discharge profiles of a few selected cycles at different specific currents and upon cycling at 2000 mA g^{-1} are displayed in Fig. S5. The CVO/GO composite exhibits satisfactory properties as cathode material and is ideally suited to serve as a model compound for the investigation of the intercalation mechanism.

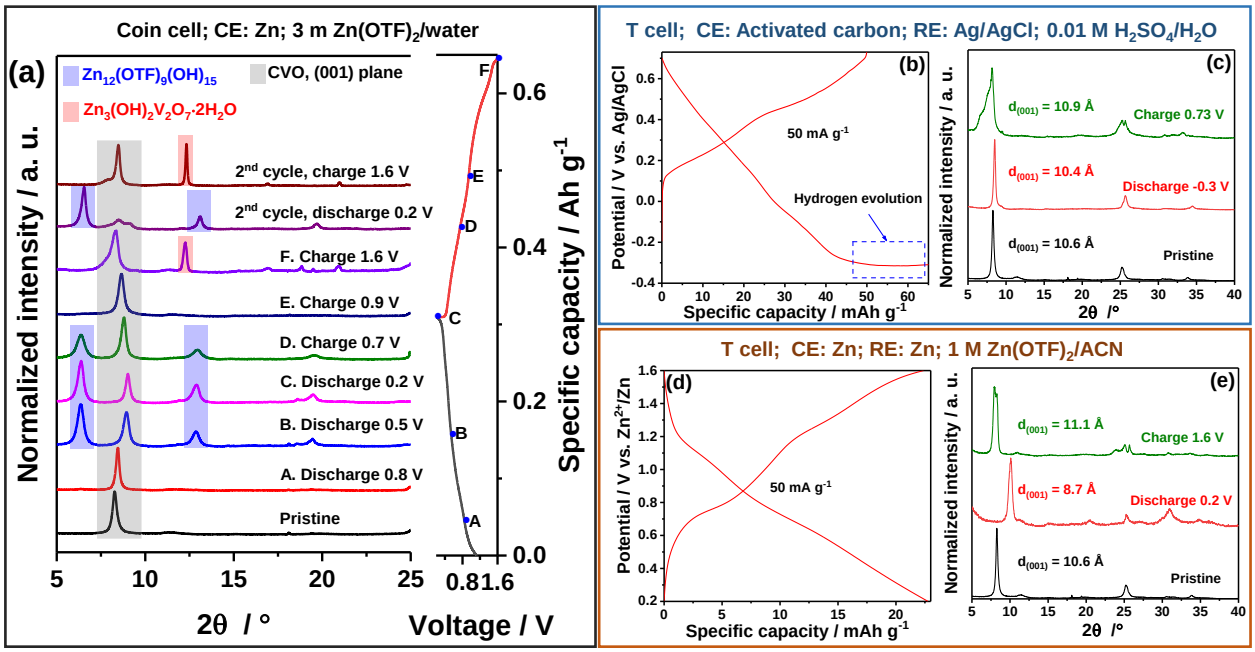

Figure 2. *(a) Ex situ XRD patterns of cycled CVO/GO electrodes at different state of charge (A-F) during the first cycle and fully charged and fully discharged during the second cycle (coin cell, 3 m $Zn(OTF)_2$ aqueous electrolyte). Charge/discharge profiles and ex situ XRD patterns at different states of charge of CVO/GO electrodes in (b and c) 0.01 M H_2SO_4/H_2O and (d and e) 1 M $Zn(OTF)_2$/ACN electrolytes, respectively. CE is counter electrode. RE is reference electrode.*

Following the exploration route in earlier works, we start with the *ex situ* XRD characterization of the CVO/GO electrode in $Zn(OTF)_2$ aqueous electrolyte. Fig. 2a displays the XRD patterns of CVO/GO electrodes at different states of charge during the first two cycles, as well as the voltage-capacity profile during the first cycle. The electrodes were unmounted from the cells and washed with MilliQ water. Upon charge and discharge, the XRD patterns exhibit a reversible shift of the CVO's (001) reflection. Moreover, additional peaks appear/disappear during cycling, suggesting the formation of additional phases. The reversible shift of the (001) plane of CVO indicates a typical solid solution mechanism, originating from cation intercalations. Due to their opposite charge, V-O layers and intercalated cations attract each other, thus leading to a decrease of the interlayer distance from 10.6 Å to 9.8 Å during the discharge process and an expansion back to

10.6 Å during the subsequent charge process. At high voltage, an additional reflection appearing at 12.3° can be indexed to the (001) plane of $Zn_3(OH)_2V_2O_7{\cdot}2H_2O$ (12.29 °, PDF 50-0570). $Zn_3(OH)_2V_2O_7{\cdot}2H_2O$ has been investigated as an intercalation cathode material.[40,41] However, this peak disappears in the next discharge, thus attributed in literature to the dissolution of vanadium in aqueous electrolyte.[28] At low voltage (0.2–0.5 V in discharge, and 0.2– 0.7 V in charge), a series of peaks at 6.4°, 12.9°, 19.5° (highlighted in blue) can be indexed to $Zn_{12}(CF_3SO_3)_9(OH)_{15}{\cdot}xH_2O$ according to previous works.[31,32] The SEM image of the fully discharged CVO/GO electrode (F) evidences that the initially porous electrode is covered by a dense layer (Fig. S6). XPS toward the same electrode evidences peaks in the O 1s region associated with –OH, -S=O and –S-O species, while the V 2p and Ca 2p core-level are not visible (Fig. S3). These results well prove the reversible formation of $Zn_{12}(CF_3SO_3)_9(OH)_{15}{\cdot}xH_2O$, which is a good indicator for H^+ intercalation occurring in the low voltage region (0.2-0.5 V) upon discharge. Yet, the involvement of H^+ in the higher voltage region as well as of Zn^{2+} ions along the entire discharge and charge processes are still unclear. Despite the presence of $Zn_3(OH)_2V_2O_7{\cdot}2H_2O$, which is associated with vanadium dissolution,[28] the energy storage mechanism of CVO is mainly based on solid solution processes. Although a variation of the diffusion coefficient upon charge/discharge is observed (Fig. S7), this cannot be used to distinguish the shuttling cation (Zn^{2+}, H^+), as discussed in SI.

To further clarify the role of H^+ and Zn^{2+} intercalation in CVO, three-electrode Swagelok-type T cells employing either 0.01 M H_2SO_4 aqueous solution or 1 M $Zn(OTF)_2$ in ACN as the electrolyte were assembled. Because the higher concentration of H_2SO_4 leads to higher on-set potential of hydrogen evolution and the solubility $Zn(OTF)_2$ in ACN is limited, higher concentrations of the electrolytes were not applied. For the H^+ intercalation investigation, free-standing activated carbon (AC) electrodes and leakless Ag/AgCl electrodes were used as the

counter and reference electrodes, respectively, to exclude the influence of Zn^{2+}. Due to the limited electrochemical stability window of the 0.01 M H_2SO_4 aqueous solution, severe irreversible hydrogen evolution is observed in the discharge curve shown in Fig. 2b. Nonetheless, even within the narrow potential window (-0.3–0.73 V vs. Ag/AgCl, corresponding to 0.57–1.6 V vs. Zn^{2+}/Zn), the CVO/GO electrode uptakes H^+ up to 45 mAh g^{-1} as observed in the following charge. In the XRD patterns of the CVO/GO electrode discharged to -0.3 V vs. Ag/AgCl and charged to 0.73 V vs. Ag/AgCl (Fig. 2c), only peaks belonging to CVO can be observed. The (001) reflection exhibits a typical lattice breath, which proves the solid solution process to occur for CVO in 0.01 M H_2SO_4. For the investigation of Zn^{2+} intercalation in CVO, cells employing Zn foils as both the counter and the reference electrodes and 1 M $Zn(OTF)_2$ in ACN as the electrolyte were used. Although with a lower specific capacity (22 mAh g^{-1}) and a stronger shift of the (001) peak (see Fig. 2 d and e), the CVO/GO electrode clearly shows Zn^{2+} storage ability. From the results mentioned above, H^+ and Zn^{2+} can be independently intercalated into CVO through solid solution processes. However, the observed capacity values for each of these two ions cannot be directly transferred to the Zn/CVO cell using 3 m $Zn(OTF)_2$ aqueous solution (Fig. 1 c and f) because of the inherent differences between the employed electrolytes and cells.

Overall, a lack of effective characterization tools to discriminate the H^+ and Zn^{2+} intercalation processes appears in the Zn/CVO cell using 3 m $Zn(OTF)_2$ aqueous solution. In fact, the intercalation of both H^+ and Zn^{2+} occurs via solid solution processes, which eliminates the support of XRD, as well as high-resolution transmission electron microscope (both supplying interlayer distances according to their operation mechanisms). On the other hand, the formation of the BZSs containing Zn species but not related to Zn^{2+} intercalation in CVO, cuts out all elemental analysis techniques, e.g., XPS, EDS, and inductively coupled plasma atomic emission.

However, it is important to state that intercalated H^+ must originate from the 3 m $Zn(OTF)_2$ aqueous electrolyte. This means that an increase of the electrolyte's pH occurs when H^+ are intercalated in CVO, but not upon Zn^{2+} intercalation. Therefore, monitoring the electrolyte's pH appears to be an appropriate, indirect tool to discriminate the H^+ and Zn^{2+} intercalation processes. Surprisingly, *in situ* or *operando* pH measurements in Zn/vanadium oxide AZMBs have not been reported before to the best of our knowledge.

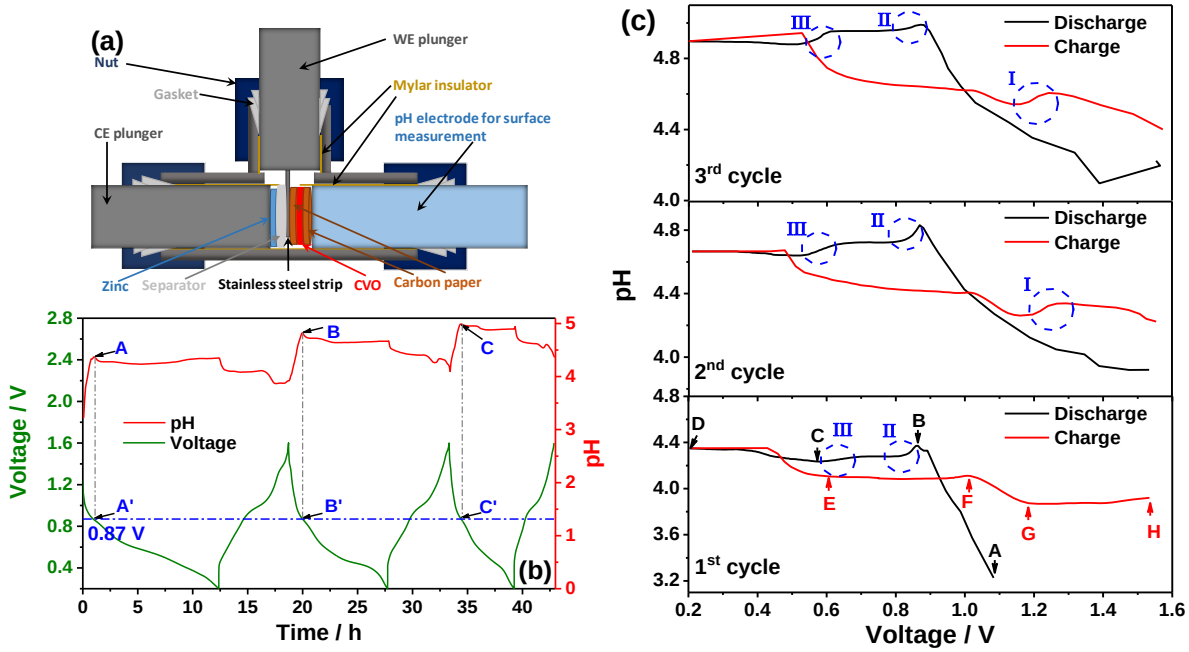

Figure 3. *(a) Scheme of the cell configuration for operando pH measurements. (b) Evolution of the cell voltage and the electrolyte pH value upon the initial three charge/discharge cycles at 50 mA* g^{-1}*. (c) Evolution of pH versus voltage during the initial three charge/discharge cycles. 3 m* $Zn(OTF)_2$ *aqueous electrolyte.*

Fig. 3a displays the scheme of the designed cell for *operando* pH measurements. A stainless steel strip and a porous carbon paper (the left one) were used as a current collector for the working electrode. This additional carbon paper disk can increase the contact of CVO electrode with the stainless steel because the size of the stainless steel and the electronic conductivity of CVO are limited. CVO/GO slurry cast on another porous carbon paper (the right one) was applied as a

working electrode with the active material side facing the current collector. The backside of the electrode, the porous carbon paper substrate, was in direct contact with a pH electrode that has a flat membrane and therefore can measure the pH value of the electrolyte on the carbon paper surface. The use of this configuration guarantees a high sensitivity of the pH measurement, because it detects in close contact of the active material.[42] Moreover, the limited amount of electrolyte (only 100 μL) used in this cell guarantees a significant variation of pH, which is not achievable in the beaker cell's configuration.[43] The cell was subjected to GCPL test at 50 mA g^{-1} while the pH value was recorded with a pH meter every 5 min. Fig. 3b displays the typical evolution of the cell voltage and electrolyte pH during the initial three cycles. The cycling performance of the CVO electrode in this *operando* cell is slightly inferior compared to that obtained in the coin cell tests. Lower efficiency and reversibility are detected, but associated with the imperfect configuration of the *operando* cell. The limited reversibility of CVO in the *operando* cell and the hydrogen evolution on Zn metal negative electrodes[6] can explain the drift of the pH value, which does not recover to its initial value after each cycle. However, the correlation of the pH variation with the cell voltage upon cycling is very evident, demonstrating that the pH variation is tightly associated with the electrochemical reaction of the CVO.

At the beginning of the discharge process, a sharp increase of the pH value is observed (see Fig. 3b). Despite the pH drift affecting the absolute value, the same occurs in the following discharges and always ends at around 0.87 V, once more implying a strong correlation between pH and voltage. To have a better overview of the relation between the voltage and the pH, Fig. 3c illustrates the pH versus voltage trend upon each cycle. In the first discharge, two regions (A-B and C-D) can be identified by increasing pH values, while one region (B-C) shows a rather stable pH. Increasing pH values can be results of the intercalation of H^+ into CVO or/and hydrogen evolution,

oxygen reduction side reactions. In the plateau region (B-C), accounting for a significant fraction of the CVO's capacity (about 35%), the stability of the pH value excludes H^+ intercalation. Hence, Zn^{2+} intercalation is most likely taking place in this region. The noninfluence of Zn^{2+} intercalation in pH evolution can also be extended to the de-intercalation of Zn^{2+} upon the charging process.

Similarly, in the first charge process, two regions (D-E and F-G) are characterized by decreasing pH values, while two other regions (E-F and G-H) evidence a steady pH. The E-F region can be associated with the de-intercalation of Zn^{2+} ions, previously intercalated in the B-C region. The G-H region, i.e., above 1.2 V, is related to the de-intercalation of Ca^{2+} ions from the CVO (see Fig. S3 and related text in SI). One can conclude that de-intercalation of H^+ ions from CVO is the only reason leading to the pH decrease in these two regions (D-E and F-G), because of the following two reasons:

(i) The voltage of these two regions is much lower than the on-set potential of oxygen evolution reaction in 3 m $Zn(OTF)_2$ aqueous electrolyte (higher than 2.3 V vs. Zn^{2+}/Zn);[44]

(ii) It has been evidenced that the intercalation/de-intercalation of Zn^{2+} does not significantly affect the measured pH.

The pH decrease in the D-E and F-G regions (charge) well relates to the pH increase in regions A-B and C-D (discharge), taking place at the same voltage. Therefore, the occurrence of de-intercalation of H^+ in D-E and F-G regions also indicates the presence of H^+ intercalation into CVO in regions A-B and C-D. In the C-D and D-E regions, the formation and disappearance of $Zn_{12}(CF_3SO_3)_9(OH)_{15}\cdot xH_2O$ occur (see above), which can now be unambiguously related to the pH increase (C-D) and decrease (D-E).

These results indicate that both the H^+ and Zn^{2+} intercalations take place and contribute to the specific capacity of CVO in AZMBs. However, the contribution of Zn^{2+} intercalation/release in the regions where the pH varies, e.g., A-B, C-D, D-E, and F-G, cannot be excluded.

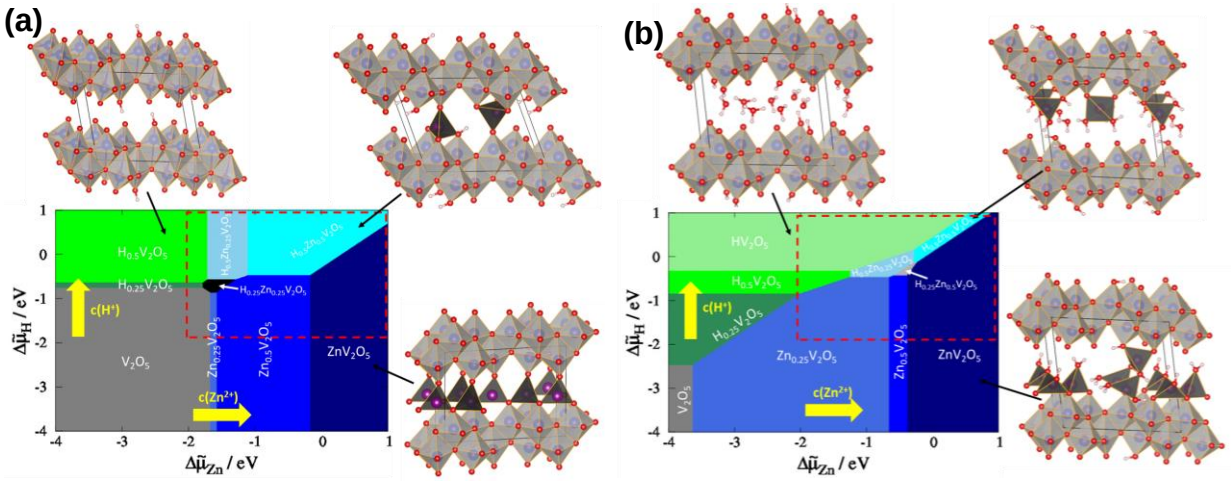

Figure 4. *Calculated phase diagrams for hydrogen and Zn intercalation in (a) water-free δ-V_2O_5 and (b) δ-V_2O_5·H_2O as a function of the respective electrochemical potential. The stoichiometry of the stable phases is denoted in the corresponding area of the phase diagram. Structure images depicting hydrogen intercalation, Zn intercalation, and hydrogen-Zn co-intercalation are exemplary shown next to the respective regions of the phase diagram. The dashed red box is a rough estimate of the chemical potential range relevant to the experiment. The yellow arrows point in the direction of increasing Zn^{2+} and H^+ concentration (i.e., decreasing pH).*

Upon the following (2nd and 3rd) cycles, the pH evolution is generally similar to that observed in the first cycle, apart from region I (blue circle in Fig. 3 b), in which the pH is seen to increase upon charge. In fact, the intercalated H^+ and Zn^{2+} cations should be released back into the electrolyte during charge. However, the increasing pH value supports for H^+ intercalation. This phenomenon is also observed in the third cycle. Moreover, in regions II and III (also marked with blue circles in the discharge processes), the pH decreases rather than stabilizes or increases. These imply that the Zn^{2+} de-intercalation in region I is accompanied by H^+ intercalation, while the Zn^{2+}

intercalation in regions II and III is accompanied by H^+ de-intercalation. Such an H^+/Zn^{2+}-exchange has seldom been reported in battery systems. DFT calculations were performed to gain insights into the mechanism being responsible for this unusual intercalation chemistry. For this purpose, a large number of model structures with different intercalation chemistry were optimized by applying the VASP code (see SI for details).[45,46]

As the Ca^{2+} is released into the electrolyte during the first charge (Fig. S4), δ-V_2O_5, i.e., the V-O skeleton of CVO, was used. In a first approach, structural water was neglected, meaning that only the intercalation of H^+ and Zn^{2+} ions was considered. Interestingly, for this scenario, Zn prefers to be tetrahedrally coordinated by oxygen atoms from the V_2O_5 layers, while hydrogen coordinates on the V-O layers trying to maximize its distance to the next Zn atom (Fig. S9). This is exemplarily shown for three different compounds (see Fig. 4a). Moreover, it is observed that the structural integrity of the layers is lost when more than 0.5 H^+/f.u. (formula unit of V_2O_5) are inserted, while the intercalation of one Zn^{2+}/f.u. is still possible. The concept of the computational hydrogen electrode (CHE) was adapted to access the respective stability of the intercalation compounds in an electrochemical environment.[47,48] With this approach, it is possible to access the phase stability with respect to the electrochemical potential, however, without having to explicitly calculate solvated ions (see SI for a detailed discussion). Hence, this allows constructing a phase diagram as a function of the zinc and hydrogen electrochemical potentials ($\Delta\tilde{\mu}_{Zn}$ and $\Delta\tilde{\mu}_{H}$, respectively), which depend on the temperature, pressure, and corresponding ion concentrations (e.g., Zn^{2+} and H^+). The phase diagram obtained with this approach is depicted in Fig. 5a. Taking a closer look at the phase boundaries of the respective phases, reveals that, depending on the electrochemical potential, different intercalation compounds are stable. In this graph, an increasing H^+ concentration (decreasing pH) and otherwise unchanged parameters, corresponds to

displacement along the y-axis. Hence, many regions are seen in the phase diagram for which an increasing pH value will indeed result in H^+ moving out from the structure, while Zn^{2+} will move in. This obviously corresponds to the experimentally observed exchange mechanism.

In a subsequent step, the structural water has been introduced in the DFT model, thus allowing for a more realistic modeling of the intercalation process. The investigated host structure is δ-$V_2O_5 \cdot H_2O$. Indeed, when water is present in the structure, H^+ ions either form H_3O^+ ions with the structural water, or coordinate on the V-O layers as in the water-free scenario (see Fig. 4b and Fig. S10). However, now the structure can accept more than 1 H^+/f.u., which is clearly a consequence of the structural water. Zn^{2+}, on the other hand, mostly occurs in fourfold or fivefold environments. The oxygen from the V-O layers and structural water are involved in the coordination, as depicted in Fig. 4b. Interestingly, at high Zn contents, it is observed that even dissociation of structural water is possible, resulting in the formation of O-H groups in the coordination polyhedra of the Zn^{2+} (see Fig. 4b). Revisiting the phase diagram it is observed that the phase fractions and the potential ranges in which they occur have changed; however, the overall trend remains the same. Still, several phase boundaries are observed that will result in an exchange of H^+ and Zn^{2+} when they are crossed, which can also explain the anomalous occurrence of a Zn^{2+} intercalation step between two H^+ intercalation steps. As a side note, it must be mentioned that different orderings and further Zn^{2+} to H^+ ratios may produce additional phases, which are stable in certain regions of the phase diagram. Similarly, changing the water content will also affect the details of the phase diagram. However, phase boundaries that result in H^+/Zn^{2+} exchange will always be present, and therefore our findings strongly corroborate the proposed exchange mechanism.

In summary, CVO/GO composites with satisfactory electrochemical performance as cathode material for AZMBs have been prepared via a highly efficient microwave reaction. With selected

electrolytes and designed cell configurations, it was proved that both Zn^{2+} and H^+ can independently intercalate into CVO. *Operando* pH measurements were employed to witness the intercalation of both H^+ and Zn^{2+} into CVO from Zn^{2+}-based aqueous electrolyte, further revealing an unusual H^+/Zn^{2+}-exchange mechanism upon charge and discharge. DFT calculations revealed that such an unusual H^+/Zn^{2+} exchange is a consequence of the variation of the electrochemical potential of Zn^{2+} and H^+ during the electrochemical intercalation/release.

ASSOCIATED CONTENT

Supporting Information

Calculation Experimental details; Computational details; Evolution of temperature and power during microwave reactions; Crystal structure scheme of CVO; EDS mapping of CVO/GO; XPS spectra of CVO/GO electrodes at different charge states; Cycling ability of the CVO/GO at 500 mA g^{-1}; Selected charge-discharge profiles of the CVO/GO; SEM images of the CVO/GO electrodes at different charge states; GITT and slow scan rate CV of the CVO/GO; Energetically most stable structures of δ-V_2O_5/δ-$V_2O_5 \cdot H_2O$ with different H^+ and Zn^{2+} contents.

AUTHOR INFORMATION

E-mail: giuseppe.elia@kit.edu; stefano.passerini@kit.edu

Notes

The authors declare no competing financial interest.

ACKNOWLEDGMENT

The authors acknowledge support by the Helmholtz Association, the state of Baden-Württemberg through bwHPC and the German Research Foundation (DFG) through grant no

INST 40/467-1 FUGG (JUSTUS cluster). The research leading to these results has received funding from the H2020 Programme (H2020-FETOPEN-2018-2019-2020) under grant agreement nº 828902, Project "VIDICAT Versatile Ionomers for Divalent Calcium Batteries". Parts of this work were performed on the supercomputer for HLR funded by the Ministry of Science, Research and the Arts Baden-Württemberg and by the Federal Ministry of Education and Research. X.L. also acknowledges financial support from the China Scholarship Council (CSC) and MZ Basque Government for her postdoctoral fellowship.

REFERENCES

(1) Tang, B.; Shan, L.; Liang, S.; Zhou, J. Issues and Opportunities Facing Aqueous Zinc-Ion Batteries. *Energy Environ. Sci.* **2019**, *12* (11), 3288–3304. https://doi.org/10.1039/c9ee02526j.

(2) Qiu, H.; Du, X.; Zhao, J.; Wang, Y.; Ju, J.; Chen, Z.; Hu, Z.; Yan, D.; Zhou, X.; Cui, G. Zinc Anode-Compatible in-Situ Solid Electrolyte Interphase via Cation Solvation Modulation. *Nat. Commun.* **2019**, *10* (1). https://doi.org/10.1038/s41467-019-13436-3.

(3) Song, M.; Tan, H.; Chao, D.; Fan, H. J. Recent Advances in Zn-Ion Batteries. *Adv. Funct. Mater.* **2018**, *28* (41), 1–27. https://doi.org/10.1002/adfm.201802564.

(4) Fang, G.; Zhou, J.; Pan, A.; Liang, S. Recent Advances in Aqueous Zinc-Ion Batteries. *ACS Energy Lett.* **2018**, *3* (10), 2480–2501. https://doi.org/10.1021/acsenergylett.8b01426.

(5) Zhang, N.; Jia, M.; Dong, Y.; Wang, Y.; Xu, J.; Liu, Y.; Jiao, L.; Cheng, F. Hydrated Layered Vanadium Oxide as a Highly Reversible Cathode for Rechargeable Aqueous Zinc Batteries. *Adv. Funct. Mater.* **2019**, *29* (10), 1–9. https://doi.org/10.1002/adfm.201807331.

(6) Zhao, Z.; Zhao, J.; Hu, Z.; Li, J.; Li, J.; Zhang, Y.; Wang, C.; Cui, G. Long-Life and Deeply Rechargeable Aqueous Zn Anodes Enabled by a Multifunctional Brightener-Inspired

Interphase. *Energy Environ. Sci.* **2019**, *12* (6), 1938–1949. https://doi.org/10.1039/c9ee00596j.

(7) Liu, X.; Zhang, H.; Geiger, D.; Han, J.; Varzi, A.; Kaiser, U.; Moretti, A.; Passerini, S. Calcium Vanadate Sub-Microfibers as Highly Reversible Host Cathode Material for Aqueous Zinc-Ion Batteries. *Chem. Commun.* **2019**, *55* (16), 2265–2268. https://doi.org/10.1039/c8cc07243d.

(8) Kundu, D.; Adams, B. D.; Duffort, V.; Vajargah, S. H.; Nazar, L. F. A High-Capacity and Long-Life Aqueous Rechargeable Zinc Battery Using a Metal Oxide Intercalation Cathode. *Nat. Energy* **2016**, *1* (10), 1–8. https://doi.org/10.1038/nenergy.2016.119.

(9) Chen, L.; An, Q.; Mai, L. Recent Advances and Prospects of Cathode Materials for Rechargeable Aqueous Zinc-Ion Batteries. *Adv. Mater. Interfaces* **2019**, *6* (17), 1–24. https://doi.org/10.1002/admi.201900387.

(10) Konarov, A.; Voronina, N.; Jo, J. H.; Bakenov, Z.; Sun, Y. K.; Myung, S. T. Present and Future Perspective on Electrode Materials for Rechargeable Zinc-Ion Batteries. *ACS Energy Lett.* **2018**, *3* (10), 2620–2640. https://doi.org/10.1021/acsenergylett.8b01552.

(11) Zhu, K.; Wu, T.; Huang, K. NaCa0.6V6O16·3H2O as an Ultra-Stable Cathode for Zn-Ion Batteries: The Roles of Pre-Inserted Dual-Cations and Structural Water in V3O8 Layer. *Adv. Energy Mater.* **2019**, *9* (38), 1–12. https://doi.org/10.1002/aenm.201901968.

(12) Liao, M.; Wang, J.; Ye, L.; Sun, H.; Wen, Y.; Wang, C.; Sun, X.; Wang, B.; Peng, H. A Deep-Cycle Aqueous Zinc-Ion Battery Containing an Oxygen-Deficient Vanadium Oxide Cathode. *Angew. Chemie - Int. Ed.* **2019**, 2273–2278. https://doi.org/10.1002/anie.201912203.

(13) Liu, F.; Chen, Z.; Fang, G.; Wang, Z.; Cai, Y.; Tang, B.; Zhou, J.; Liang, S. V2O5

Nanospheres with Mixed Vanadium Valences as High Electrochemically Active Aqueous Zinc-Ion Battery Cathode. *Nano-Micro Lett.* **2019**, *11* (1), 1–11. https://doi.org/10.1007/s40820-019-0256-2.

(14) Chen, L.; Yang, Z.; Huang, Y. Monoclinic VO2(D) Hollow Nanospheres with Super-Long Cycle Life for Aqueous Zinc Ion Batteries. *Nanoscale* **2019**, *11* (27), 13032–13039. https://doi.org/10.1039/c9nr03129d.

(15) Pan, Z.; Yang, J.; Yang, J.; Zhang, Q.; Zhang, H.; Li, X.; Kou, Z.; Zhang, Y.; Chen, H.; Yan, C.; et al. Stitching of Zn3(OH)2V2O7·2H2O 2D Nanosheets by 1D Carbon Nanotubes Boosts Ultrahigh Rate for Wearable Quasi-Solid-State Zinc-Ion Batteries. *ACS Nano* **2020**, *14*, 842–853. https://doi.org/10.1021/acsnano.9b07956.

(16) Liu, Y.; Li, Q.; Ma, K.; Yang, G.; Wang, C. Graphene Oxide Wrapped Cuv2o6 Nanobelts as High-Capacity and Long-Life Cathode Materials of Aqueous Zinc-Ion Batteries. *ACS Nano* **2019**, *13* (10), 12081–12089. https://doi.org/10.1021/acsnano.9b06484.

(17) Wan, F.; Niu, Z. Design Strategies for Vanadium-Based Aqueous Zinc-Ion Batteries. *Angew. Chemie - Int. Ed.* **2019**, *58* (46), 16358–16367. https://doi.org/10.1002/anie.201903941.

(18) Yan, M.; He, P.; Chen, Y.; Wang, S.; Wei, Q.; Zhao, K.; Xu, X.; An, Q.; Shuang, Y.; Shao, Y.; et al. Water-Lubricated Intercalation in V2O5·nH2O for High-Capacity and High-Rate Aqueous Rechargeable Zinc Batteries. *Adv. Mater.* **2018**, *30* (1), 1–6. https://doi.org/10.1002/adma.201703725.

(19) Soundharrajan, V.; Sambandam, B.; Kim, S.; Alfaruqi, M. H.; Putro, D. Y.; Jo, J.; Kim, S.; Mathew, V.; Sun, Y. K.; Kim, J. Na2V6O16·3H2O Barnesite Nanorod: An Open Door to Display a Stable and High Energy for Aqueous Rechargeable Zn-Ion Batteries as Cathodes.

Nano Lett. **2018**, *18* (4), 2402–2410. https://doi.org/10.1021/acs.nanolett.7b05403.

(20) Ming, F.; Liang, H.; Lei, Y.; Kandambeth, S.; Eddaoudi, M.; Alshareef, H. N. Layered Mg XV2O5· NH2O as Cathode Material for High-Performance Aqueous Zinc Ion Batteries. *ACS Energy Lett.* **2018**, *3* (10), 2602–2609. https://doi.org/10.1021/acsenergylett.8b01423.

(21) Li, Z.; Ganapathy, S.; Xu, Y.; Zhou, Z.; Sarilar, M.; Wagemaker, M. Mechanistic Insight into the Electrochemical Performance of Zn/VO2 Batteries with an Aqueous ZnSO4 Electrolyte. *Adv. Energy Mater.* **2019**, *9* (22), 1–10. https://doi.org/10.1002/aenm.201900237.

(22) Pang, Q.; Sun, C.; Yu, Y.; Zhao, K.; Zhang, Z.; Voyles, P. M.; Chen, G.; Wei, Y.; Wang, X. H2V3O8 Nanowire/Graphene Electrodes for Aqueous Rechargeable Zinc Ion Batteries with High Rate Capability and Large Capacity. *Adv. Energy Mater.* **2018**, *8* (19), 1–9. https://doi.org/10.1002/aenm.201800144.

(23) Sambandam, B.; Soundharrajan, V.; Kim, S.; Alfaruqi, M. H.; Jo, J.; Kim, S.; Mathew, V.; Sun, Y. K.; Kim, J. Aqueous Rechargeable Zn-Ion Batteries: An Imperishable and High-Energy Zn2V2O7 Nanowire Cathode through Intercalation Regulation. *J. Mater. Chem. A* **2018**, *6* (9), 3850–3856. https://doi.org/10.1039/c7ta11237h.

(24) Kundu, D.; Hosseini Vajargah, S.; Wan, L.; Adams, B.; Prendergast, D.; Nazar, L. F. Aqueous: Vs. Nonaqueous Zn-Ion Batteries: Consequences of the Desolvation Penalty at the Interface. *Energy Environ. Sci.* **2018**, *11* (4), 881–892. https://doi.org/10.1039/c8ee00378e.

(25) Liu, W.; Dong, L.; Jiang, B.; Huang, Y.; Wang, X.; Xu, C.; Kang, Z.; Mou, J.; Kang, F. Layered Vanadium Oxides with Proton and Zinc Ion Insertion for Zinc Ion Batteries. *Electrochim. Acta* **2019**, *320*, 134565. https://doi.org/10.1016/j.electacta.2019.134565.

(26) He, P.; Quan, Y.; Xu, X.; Yan, M.; Yang, W.; An, Q.; He, L.; Mai, L. High-Performance Aqueous Zinc–Ion Battery Based on Layered H2V3O8 Nanowire Cathode. *Small* **2017**, *13* (47), 1–7. https://doi.org/10.1002/smll.201702551.

(27) He, P.; Zhang, G.; Liao, X.; Yan, M.; Xu, X.; An, Q.; Liu, J.; Mai, L. Sodium Ion Stabilized Vanadium Oxide Nanowire Cathode for High-Performance Zinc-Ion Batteries. *Adv. Energy Mater.* **2018**, *8* (10), 1–6. https://doi.org/10.1002/aenm.201702463.

(28) Zhang, L.; Rodríguez-Pérez, I. A.; Jiang, H.; Zhang, C.; Leonard, D. P.; Guo, Q.; Wang, W.; Han, S.; Wang, L.; Ji, X. ZnCl2 "Water-in-Salt" Electrolyte Transforms the Performance of Vanadium Oxide as a Zn Battery Cathode. *Adv. Funct. Mater.* **2019**, *29* (30), 1–6. https://doi.org/10.1002/adfm.201902653.

(29) Alfaruqi, M. H.; Mathew, V.; Song, J.; Kim, S.; Islam, S.; Pham, D. T.; Jo, J.; Kim, S.; Baboo, J. P.; Xiu, Z.; et al. Electrochemical Zinc Intercalation in Lithium Vanadium Oxide: A High-Capacity Zinc-Ion Battery Cathode. *Chem. Mater.* **2017**, *29* (4), 1684–1694. https://doi.org/10.1021/acs.chemmater.6b05092.

(30) Wan, F.; Zhang, L.; Dai, X.; Wang, X.; Niu, Z.; Chen, J. Aqueous Rechargeable Zinc/Sodium Vanadate Batteries with Enhanced Performance from Simultaneous Insertion of Dual Carriers. *Nat. Commun.* **2018**, *9* (1), 1–11. https://doi.org/10.1038/s41467-018-04060-8.

(31) Li, Q.; Liu, Y.; Ma, K.; Yang, G.; Wang, C. In Situ Ag Nanoparticles Reinforced Pseudo-Zn – Air Reaction Boosting Ag 2 V 4 O 11 as High-Performance Cathode Material for Aqueous Zinc-Ion Batteries. **2019**, *1900637*, 1–8. https://doi.org/10.1002/smtd.201900637.

(32) Yang, G.; Li, Q.; Ma, K.; Hong, C.; Wang, C. The Degradation Mechanism of Vanadium Oxide-Based Aqueous Zinc-Ion Batteries. **2020**, 8084–8095.

https://doi.org/10.1039/d0ta00615g.

(33) Wei, T.; Li, Q.; Yang, G.; Wang, C. Pseudo-Zn – Air and Zn-Ion Intercalation Dual Mechanisms to Realize High-Areal Capacitance and Long-Life Energy Storage in Aqueous Zn Battery. **2019**, *1901480*, 1–7. https://doi.org/10.1002/aenm.201901480.

(34) Park, M. J.; Yaghoobnejad Asl, H.; Manthiram, A. Multivalent-Ion versus Proton Insertion into Battery Electrodes. *ACS Energy Lett.* **2020**, 2367–2375. https://doi.org/10.1021/acsenergylett.0c01021.

(35) Canepa, P.; Sai Gautam, G.; Hannah, D. C.; Malik, R.; Liu, M.; Gallagher, K. G.; Persson, K. A.; Ceder, G. Odyssey of Multivalent Cathode Materials: Open Questions and Future Challenges. *Chem. Rev.* **2017**, *117* (5), 4287–4341. https://doi.org/10.1021/acs.chemrev.6b00614.

(36) Zhou, W.; Chen, J.; He, C.; Chen, M.; Xu, X.; Tian, Q.; Xu, J.; Wong, C. P. Hybridizing δ-Type NaxV2O5·nH2O with Graphene towards High-Performance Aqueous Zinc-Ion Batteries. *Electrochim. Acta* **2019**, *321*, 2–10. https://doi.org/10.1016/j.electacta.2019.134689.

(37) Clites, M.; Hart, J. L.; Taheri, M. L.; Pomerantseva, E. Chemically Preintercalated Bilayered KxV2O5· n H2O Nanobelts as a High-Performing Cathode Material for K-Ion Batteries. *ACS Energy Lett.* **2018**, *3* (3), 562–567. https://doi.org/10.1021/acsenergylett.7b01278.

(38) Clites, M.; Pomerantseva, E. Bilayered Vanadium Oxides by Chemical Pre-Intercalation of Alkali and Alkali-Earth Ions as Battery Electrodes. *Energy Storage Mater.* **2018**, *11* (May 2017), 30–37. https://doi.org/10.1016/j.ensm.2017.09.005.

(39) Xia, C.; Guo, J.; Li, P.; Zhang, X.; Alshareef, H. N. Highly Stable Aqueous Zinc-Ion

Storage Using a Layered Calcium Vanadium Oxide Bronze Cathode. *Angew. Chemie* **2018**, *130* (15), 4007–4012. https://doi.org/10.1002/ange.201713291.

(40) Xia, C.; Guo, J.; Lei, Y.; Liang, H.; Zhao, C.; Alshareef, H. N. Rechargeable Aqueous Zinc-Ion Battery Based on Porous Framework Zinc Pyrovanadate Intercalation Cathode. *Adv. Mater.* **2018**, *30* (5), 1–7. https://doi.org/10.1002/adma.201705580.

(41) Guo, J.; Ming, J.; Lei, Y.; Zhang, W.; Xia, C.; Cui, Y.; Alshareef, H. N. Artificial Solid Electrolyte Interphase for Suppressing Surface Reactions and Cathode Dissolution in Aqueous Zinc Ion Batteries. *ACS Energy Lett.* **2019**, *4* (12), 2776–2781. https://doi.org/10.1021/acsenergylett.9b02029.

(42) Lee, B.; Seo, R.; Lee, R.; Yoon, S.; Kim, H.; Chung, K. Y.; Cho, W.; Hyoung, S. Critical Role of PH Evolution of Electrolyte in the Reaction Mechanism for Rechargeable Zinc Batteries. **2016**, 2948–2956. https://doi.org/10.1002/cssc.201600702.

(43) Bischoff, C. F.; Fitz, S.; Burns, J.; Bauer, M.; Gentischer, H.; Birke, K. P.; Henning, H.; Biro, D. Revealing the Local PH Value Changes of Acidic Aqueous Zinc Ion Batteries with a Manganese Dioxide Electrode during Cycling Revealing the Local PH Value Changes of Acidic Aqueous Zinc Ion Batteries with a Manganese Dioxide Electrode during Cycling. **2020**. https://doi.org/10.1149/1945-7111/ab6c57.

(44) Zhang, N.; Cheng, F.; Liu, Y.; Zhao, Q.; Lei, K.; Chen, C.; Liu, X.; Chen, J. Cation-Deficient Spinel ZnMn2O4 Cathode in Zn(CF3SO3)2 Electrolyte for Rechargeable Aqueous Zn-Ion Battery. *J. Am. Chem. Soc.* **2016**, *138* (39), 12894–12901. https://doi.org/10.1021/jacs.6b05958.

(45) Kresse, G.; Furthmüller, J. Efficient Iterative Schemes for Ab Initio Total-Energy Calculations Using a Plane-Wave Basis Set. *Phys. Rev. B - Condens. Matter Mater. Phys.*

1996, *54* (16), 11169–11186. https://doi.org/10.1103/PhysRevB.54.11169.

(46) Joubert, D. From Ultrasoft Pseudopotentials to the Projector Augmented-Wave Method. *Phys. Rev. B - Condens. Matter Mater. Phys.* **1999**, *59* (3), 1758–1775. https://doi.org/10.1103/PhysRevB.59.1758.

(47) Gossenberger, F.; Roman, T.; Groß, A. Hydrogen and Halide Co-Adsorption on Pt(111) in an Electrochemical Environment: A Computational Perspective. *Electrochim. Acta* **2016**, *216*, 152–159. https://doi.org/10.1016/j.electacta.2016.08.117.

(48) Nørskov, J. K.; Rossmeisl, J.; Logadottir, A.; Lindqvist, L.; Kitchin, J. R.; Bligaard, T.; Jónsson, H. Origin of the Overpotential for Oxygen Reduction at a Fuel-Cell Cathode. *J. Phys. Chem. B* **2004**, *108* (46), 17886–17892. https://doi.org/10.1021/jp047349j.